Interplay between Aharonov-Bohm and Altshuler-Aronov-Spivak oscillations in phase-pure GaAs/InAs core/shell nanowires of different lengths

Farah Basarić,[1,2,*] Kaiwen Wang,[1,2,*] Tudor-Gabriel Dumitru,[3] Andrei Manolescu,[3] Francisco Alvarado Cesar,[4,†] Ana M. Sanchez,[4] Christoph Krause,[5] Detlev Grützmacher,[1,2,5] Alexander Pawlis,[1,2,5] and Thomas Schäpers[1,2,6,‡]

[1]*Peter Grünberg Institut (PGI-9), Forschungszentrum Jülich, 52425 Jülich, Germany*
[2]*JARA-Fundamentals of Future Information Technology, Jülich-Aachen Research Alliance, Forschungszentrum Jülich and RWTH Aachen University, 52425 Jülich, Germany*
[3]*Department of Engineering, Reykjavik University, Menntavegur 1, IS-102 Reykjavik, Iceland*
[4]*Department of Physics, University of Warwick, Coventry CV4 7AL, United Kingdom*
[5]*Peter Grünberg Institut (PGI-10), Forschungszentrum Jülich, 52425 Jülich, Germany*
[6]*Department of Material Science, Tohoku University, Aobayama 2, Aoba-ku, Sendai 980-8579, Japan*

(Received 9 June 2026; revised 11 August 2026; accepted 22 September 2026; published 9 October 2026)

In GaAs/InAs core/shell nanowires, comprising a tubular conducting shell, interference phenomena observed under an axial field and originating from closed-loop states encircling the insulating core provide an ideal platform for superconducting quantum devices that utilize effects such as Aharonov-Bohm–type or Altshuler-Aronov-Spivak–type conductance oscillations. Both effects are different in nature with respect to phase rigidity because of interference of non-time-reversed or time-reversed paths, respectively. Since their occurrence is largely governed by averaging effects, which depend on sample dimensions and the transport regime, we present a systematic study of flux-periodic oscillations of phase-pure zinc-blende GaAs/InAs core/shell nanowires as a function of gate voltage for samples with different contact separation lengths. Our analysis shows that with increasing contact separation length, averaging effects result in gradual reduction of h/e-periodic Aharonov-Bohm–type oscillations, while relative to that the $h/2e$-periodic Altshuler-Aronov-Spivak oscillations and its $h/4e$-periodic higher harmonics are enhanced. The additional phase rigidity seen in the $h/3e$-periodic oscillations is attributed to phase rigidity propagating from the neighboring lower harmonics. Our tight-binding transport simulations on nanowires of different lengths which contain only a few scattering centers confirm the experimental observations regarding the different harmonics and their phase rigidity. Together, our experimental and simulation findings indicate quasiballistic transport with persistent Aharonov-Bohm–type and phase-rigid Altshuler-Aronov-Spivak–type oscillations despite few scattering centers.

DOI: 10.1103/5x9w-pjtq

I. INTRODUCTION

Semiconductor nanowires with a tubular conducting shell provide a particularly suitable platform for superconducting quantum devices that exploit electron interference phenomena [1–5]. In this work, we investigate GaAs/InAs core/shell nanowires [6–10], which exhibit a rich mesoscopic behavior, while simultaneously offering a highly tunable system for investigating coherent electron dynamics and device functionality with strong potential for future application in more complex devices for classical and quantum computing [11–17]. A notable example is the realization of a core/shell nanowire-based Josephson junction [5], where strong coupling between superconducting electrodes and the semiconducting nanowire weak link is essential. GaAs/InAs core/shell nanowires are promising candidates for such applications because they enable the precise control of the supercurrent in the Josephson junction via field effect. Additionally, the band offset at the interface between the high-band-gap core and the low-band-gap shell effectively confines charge carriers in a tubular conductor [18–21]. As a result, the electron wave function is localized near the interface with the superconducting electrodes. Studying interference effects in this respect offers direct insight into the phase coherence and transport properties of charge carriers in tubular conducting channels, as it allows for further development of quantum information devices based on such nanostructures.

When subjected to an axial magnetic field, GaAs/InAs core/shell nanowires exhibit such interference effects, manifested as magnetic flux quantum h/e-periodic Aharonov-Bohm–type (AB) [22] and $h/2e$-periodic Altshuler-Aronov-Spivak–type (AAS) conductance oscillations [23], where h is the Planck constant, and e the elementary charge. In case of planar ring structures based on semiconducting [24,25],

*These authors contributed equally to this work.
†Present address: Facility for Electron Microscopy, The University of Birmingham, Edgbaston, Birmingham B15 2TT, United Kingdom.
‡Contact author: th.schaepers@fz-juelich.de

Published by the American Physical Society under the terms of the Creative Commons Attribution 4.0 International license. Further distribution of this work must maintain attribution to the author(s) and the published article's title, journal citation, and DOI.

metallic [26–30], and graphene [31] nanostructures, these effects originate from electron path interference. While related Aharonov-Bohm physics has also been investigated in carbon nanotubes through magnetic-field-induced modifications of the circumferential electronic states [32], the electronic transport in GaAs/InAs core/shell nanowires is governed by closed-loop states that encircle the insulating core, commonly referred to as angular momentum states [6,7]. Applying an axial magnetic field, the flux-dependent energy spectrum of their angular momentum states is revealed through h/e-periodic conductance oscillations, therefore classified as an AB-type oscillations. Commonly, they have been observed as a dominant effect in GaAs/InAs nanowires. Furthermore, in terms of electron interference framework, AAS oscillations are described as the interference of time-reversed paths. In case of GaAs/InAs nanowires, so far they have been associated with elastic disorder scattering in the diffusive transport regime [7]. Recently, however, those were also reported in highly ordered quasiballistic GaAs/InAs nanowires, mediated by a few scattering centers only [10].

Previous interference studies of such phenomena on III-V semiconductor [6–10,33,34], and topological insulator nanowires [35–38] have demonstrated the critical role of system size, crystal structure, and characteristic transport length scales in shaping these interference patterns, as well as determining the crossover conditions between AB and AAS oscillations [39]. Additional to h/e- and $h/2e$-periodic oscillations, experiments on planar quasiballistic ring nanostructures [40] and topological insulator nanowires [41] showcased higher harmonic oscillations, i.e., $h/3e$, $h/4e$, etc., periodicities. These are enabled due to large phase coherence length, which allows the electron wave function to wind around the ring perimeter several times before interference occurs. However, higher harmonics have not been reported yet in tubular semiconductor nanowires.

Recently, we investigated magnetoconductance oscillations in phase-pure GaAs/InAs core/shell nanowires [10]. Despite the short nanowire length and reported quasiballistic transport regime, we observed AAS corrections at small magnetic fields. Typically, AAS oscillations are observed in samples with a large number of interfering time-reversed paths. To address this issue and better understand the relationship between AB- and AAS-type oscillations, this study examines magnetoconductance oscillations in phase-pure GaAs/InAs core/shell nanowires grown in a similar way, with contact separation lengths ranging from 300 nm to 2 μm. This allows us to access transport scenarios with different averaging of interference phenomena. We investigate these phenomena via transversal mode of transport by measuring magnetoconductance oscillations under an axial field at low temperatures, and varying the gate voltage which probes the phase of the observed oscillations. We expect AB-type oscillations to progressively average out with increasing contact separation length, while AAS-type oscillations stabilize. Furthermore, we report the observation of higher harmonics of magnetoconductance oscillations indicating a long phase coherence length. Special attention is devoted to the origin of the observed phase rigidity and the relevant magnetic field ranges within which they occur. Our experimental results are compared to tight-binding quantum transport simulations of core/shell nanowires with different lengths. These contain only a few scattering centers based on Landauer-Büttiker formalism using KWANT [42]. The presented simulation results reveal the underlying mechanism behind the observed higher harmonics.

II. EXPERIMENTAL DETAILS

The GaAs/InAs core/shell nanowires investigated were grown by molecular beam epitaxy (MBE) via the self-catalyzed vapor-liquid-solid technique on prestructured Si(111) substrates, following the procedure reported by Jansen *et al.* [43]. The growth of the GaAs core resulted in an average radius of 65 nm, while the average thickness of the InAs shell was 30 nm. The nanowires had a typical length of 3.8 μm. Details on the growth procedure can be found in the Supplemental Material [44]. Table I presents the resulting nanowire geometries of the measured samples. A transmission electron microscopy (TEM) analysis was carried out to gain information on the crystal structure of the nanowire. Due to the interplay between hole diameter and droplet size at growth start, the growth of the nanowires was stabilized in the zinc-blende regime, featuring an excellent degree of phase purity. Figure 1(a) shows a low magnification bright field transmission electron microscopy image (BF-TEM) of a typical nanowire, where a high-resolution TEM image in Fig. 1(b) along the ⟨110⟩ direction confirms the preferred zinc-blende crystal structure.

The device fabrication required primarily the precise nanowire transferring technique using a scanning electron microscope (SEM) based micromanipulator onto a prepatterned n-doped Si(100) global backgate substrate covered with 150 nm of SiO_2 used as gate dielectric. The SEM-assisted transfer and alignment were performed using a low accelerating voltage (3 kV) and for a minimal time of electron-beam exposure to reduce possible irradiation-induced modifications of the nanowire surface. Next, the contacts were defined using electron beam lithography, followed by Ar^+ cleaning and contact finger metallization with Ti/Au. Representative examples of the measured samples are shown in Figs. 1(c) and 1(d). The low-temperature measurements were carried out in a variable temperature insert cryostat, at the base temperature of 1.3 K. A four-terminal measurement setup was utilized, except for the shortest sample, which was measured in a three-terminal configuration, by means of applying 20 nA of current between the two outer contacts, whereas the voltage drop was measured between the two inner ones. The typical contact resistance was in order of 1 kΩ. For sample A, the three-terminal measurement configuration was corrected by subtracting the residual contact resistance and the lead resistance from the measured signal. We present results of gate-dependent magnetoconductance measurements on samples with different inner contact separation lengths L_c given in Table I. The measurements were carried out under an axial magnetic field, and device gating was realized by a global back-gate.

III. RESULTS AND DISCUSSION

We examined magnetotransport in samples with varying inner contact separation L_c, with a focus on samples C and

TABLE I. Sample-specific geometric dimensions and corresponding oscillation periodicities, where L_c denotes the contact separation of the voltage probes, r_{core} the GaAs core radius, t_{shell} the InAs shell thickness, r_{tot} the total nanowire radius, $f_{h/e}$, $f_{h/2e}$, $f_{h/3e}$, and $f_{h/4e}$ the positions of the h/e-, $h/2e$-, $h/3e$-, and $h/4e$-periodic peaks on the frequency scale of the fast Fourier transform analysis (third and fourth harmonics are observed only for samples C, D, and E), and $r_{h/e}$ the corresponding measured wave-function localization radius, obtained at the base temperature of 1.3 K.

Sample	L_c (μm)	r_{core} (nm)	t_{shell} (nm)	r_{tot} (nm)	$f_{\mathrm{h/e}}$ (T^{-1})	$f_{\mathrm{h/2e}}$ (T^{-1})	$f_{\mathrm{h/3e}}$ (T^{-1})	$f_{\mathrm{h/4e}}$ (T^{-1})	$r_{\mathrm{h/e}}$ (nm)
A	0.3	56	37	93	3.6	7.2			75
B	0.5	71	25	96	3.3	6.7			72
C	0.6	65	31	96	3.0	5.9	8.5	12.1	69
D	1.8	70	27	97	3.0	6.0	9.0	12.0	69
E	2.0	63	27	90	3.1	5.8	9.0	12.0	70

E, which contain short 600-nm and long 2-μm contact separations, respectively. Analogous investigations for the other samples listed in Table I are presented in the Supplemental Material [44]. The measurements were carried out in an axial magnetic field ranging between −2 and 2 T, and under varying gate voltages V_g ranging between −3 and 3 V, in 0.1-V steps. In Figs. 2(a) and 2(b), the normalized magnetoconductance G/G_0 for samples C and E, with $G_0 = e^2/h$, reveals regular AB-type oscillations. These oscillations span the entire gate voltage range, and are consistent even upon applying a gate voltage up to −3 V, implying preservation of phase-coherent transport and a persistent ring geometry of the electron wave function upon subtle carrier depletion.

The ring-shaped wave function encloses an effective area S, which in case of our nanowires corresponds to a hexagonal cross section $S = r^2(3\sqrt{3}/2)$, where r is the circumradius of the hexagon. The oscillation period ΔB of the AB-type oscillations is associated to the nanowire cross section S via the expression $\Delta B = \Phi_0/S$, where $\Phi_0 = h/e$ is the magnetic flux quantum. For samples C and E, the extracted oscillation periods ΔB of 0.33 and 0.32 T imply a radius $r_{h/e}$ of the closed-loop wave function of around 69 and 70 nm, respectively. This confirms that the wave function is localized within the InAs shell, and is found to be the case for all the other measured samples (see Table I). Furthermore, sample E showcases smaller average conductance when compared to sample C, due to larger contact separation length.

Next, the fast Fourier transform (FFT) of the magnetoconductance oscillations was analyzed. The FFT was applied to the extracted oscillation signal $\delta G = G - \overline{G}$, where $\overline{G}$ is the slowly varying background which was subtracted from the measured conductance. The results for samples C and E presented in Figs. 2(c) and 2(d) show a clear two-peak structure over the entire gate voltage range. For sample E, the FFT spectrum was calculated after removing the slowly varying background using empirical mode decomposition, as

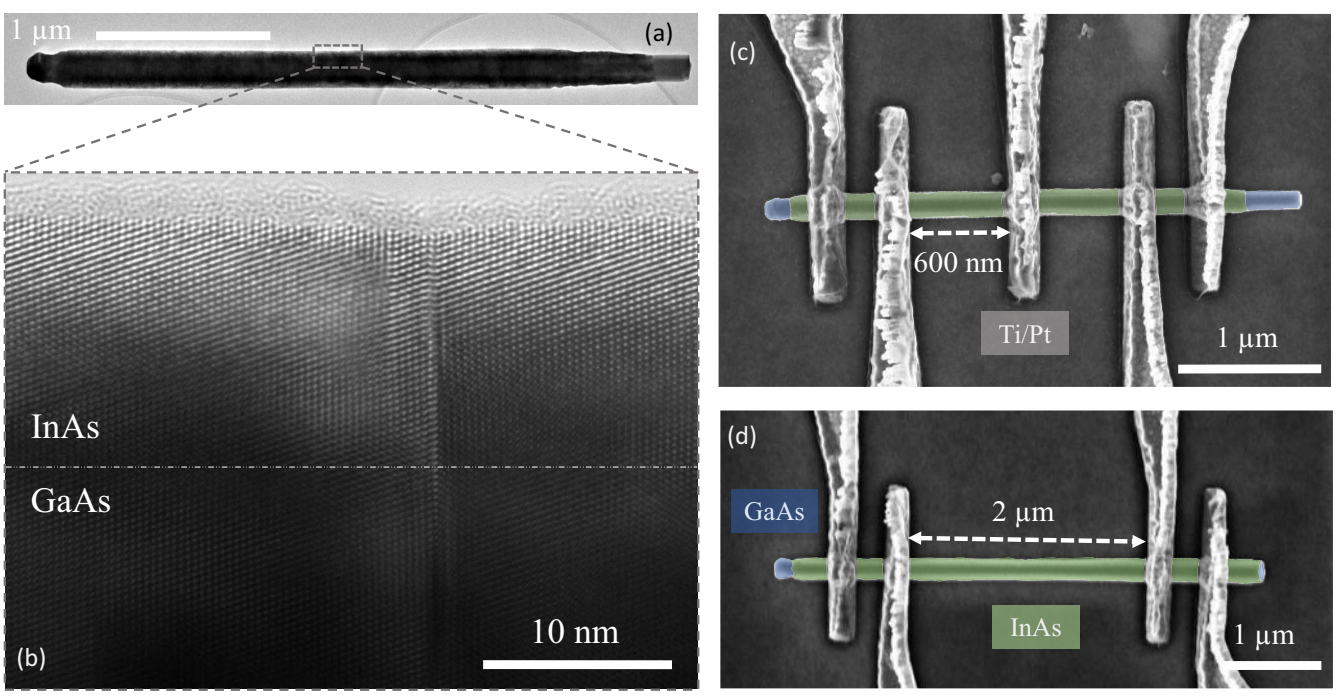

FIG. 1. (a) Low-magnification TEM image of a representative example of the GaAs/InAs nanowire, featuring (b) high-resolution TEM image of the nanowire middle region. (c) and (d) False color SEM image of samples C and E, respectively, emphasizing differences in inner contact separation lengths L_c, 600 nm and 2 μm, respectively.

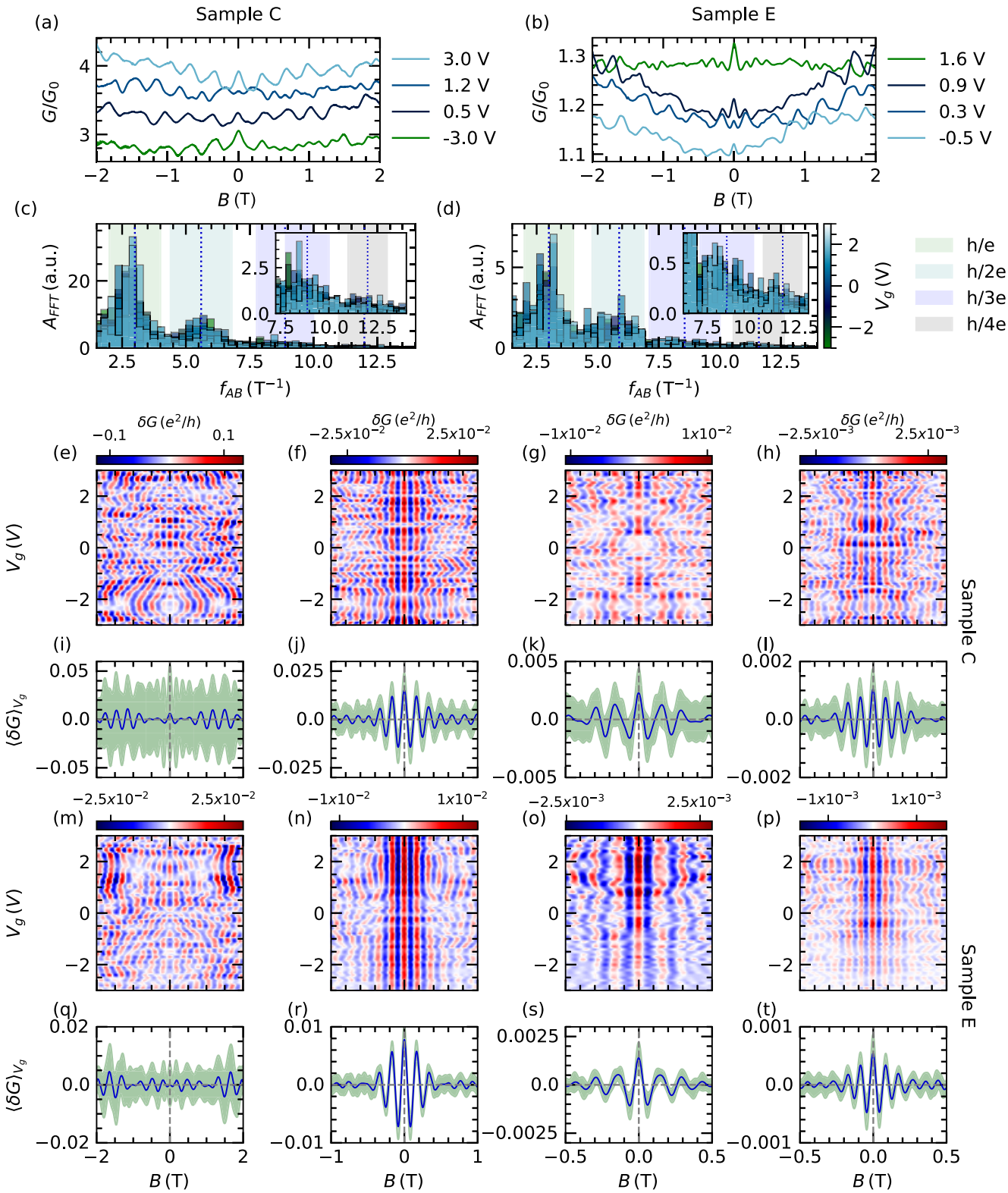

FIG. 2. Normalized magnetoconductance G/G_0, with $G_0 = e^2/h$, for various gate voltage V_g values, for (a) sample C, and (b) E, respectively. Corresponding fast-Fourier transform (FFT) of the data shown in (a) and (b), for samples (c) C and (d) E. Ranges of present harmonics (h/e, $h/2e$, $h/3e$, $h/4e$) are presented in color-coded scheme, with mean frequency value marked by dotted line. Inserts display enlarged parts of the FFT spectra corresponding to $h/3e$ and $h/4e$ contributions. Color maps for oscillation amplitude δG as a function of gate voltage and magnetic field for sample C, presented for (e) h/e-, (f) $h/2e$-, (g) $h/3e$-, and (h) $h/4e$-periodic oscillations defined by the frequency windows marked in (b). Averaged oscillation amplitude $\langle\delta G\rangle_{V_g}$ over the complete gate voltage range, as a function of magnetic field, presented with bold line, and corresponding standard deviation marked with shaded area for (i) h/e-, (j) $h/2e$-, (k) $h/3e$-, and (l) $h/4e$-periodic oscillations. Color maps in (m), (n), (o), and (p) represent analogous data analysis for sample E, shown for marked frequency ranges in (d). Averaged oscillation amplitude over gate voltage range with standard deviation of different harmonics is similarly shown for sample E in (q), (r), (s), and (t).

the raw magnetoconductance traces acquired at large negative gate voltages exhibited an elevated low-frequency noise floor that partially obscured the characteristic FFT peaks, whereas no such processing was required for sample C due to its comparatively low noise level (see Supplemental Materials for more details [44]). The first peak is associated with AB oscillations with an h/e periodicity, and the second peak corresponds to oscillations with an $h/2e$ periodicity. The latter can originate from either the second harmonics of the AB oscillations or the AAS-type oscillations. Additionally, we find indications of higher harmonics for both samples, i.e., 3rd and 4th harmonics, though with significantly smaller amplitude. However, these higher harmonics are not present consistently throughout the complete gate voltage range. In Table I, the extracted positions of these peaks imply the presence of $h/3e$- and $h/4e$-periodic oscillations. The slight broadening of the FFT peaks observed for sample E is attributed to its larger measured nanowire segment. In this case, a larger number of phase-coherent trajectories with small radius variations contribute to a broader recorded frequency spectrum. The finite magnetic-field range was also found to influence the extraction of the weak higher-order components; therefore, the full available range of $B \in (-2, 2)$ T was retained to maximize the number of oscillation periods and ensure reliable separation of the $h/3e$- and $h/4e$-periodic contributions.

Higher harmonics of AB oscillations have already been observed in other types of structures such as graphene [31], or two-dimensional electron gas heterostructure $GaAs/Ga_xAl_{1-x}As$ rings [40], as well as in Bi_2Se_3 topological insulator nanowires [41]. In these cases, the occurrence of higher harmonics stems from the system's very long phase coherence length, which allows electron partial waves to encircle the ring multiple times. However, this phenomenon has not yet been reported for GaAs/InAs core/shell nanowires. Its transport in terms of angular momentum states does not provide a straightforward explanation that aligns with the interferometric, trajectory-based framework outlined in previous studies.

To further understand the underlying physical origin of our observations, we present a quantitative study of the phase rigidity of AB and AAS oscillations and their respective higher harmonics, through varying inner contact separation lengths. For this purpose, the raw magnetoconductance signal was processed using a pair of high-pass Butterworth filters, which together effectively define a band-pass filter to isolate the frequency window corresponding to the oscillation periodicity of interest. The resulting band-limited signal was then corrected for its residual constant offset by subtracting its mean value, yielding the oscillation amplitude δG as a function of magnetic field and gate voltage. Following this method, the analysis of h/e-periodic oscillations for sample C [cf. Fig. 2(e)] reveals a nonrigid phase pattern at $B = 0$ as the gate voltage varies. The random phase shift along zero magnetic field is clearly confirmed by the solid blue line in Fig. 2(i), which illustrates the diminished averaged conductance over the voltage range $\langle \delta G \rangle_{V_g}$ at $B = 0$, whereas featuring large standard deviation marked in green at the same time. Sample E shows a similar behavior, as can be seen in Figs. 2(m) and 2(q).

Carrying out an analogous analysis for the $h/2e$-periodic oscillations, shown in Fig. 2(f), sample C reveals a phase-rigid behavior in the low magnetic field range, with a conductance maximum at $B = 0$. This observation is further supported through the analysis of $h/2e$-periodic conductance oscillations averaged over the gate voltage range [cf. Fig. 2(j)]. Here, the phase stability results in a pronounced oscillatory behavior of the averaged value extending over a magnetic field range of about ± 0.4 T, with its maximum value at $B = 0$. Additionally, the small standard deviation further confirms the observed phase rigidity. The phase-rigid part is associated with AAS conductance oscillations, as such oscillations are robust against averaging over the V_g range. The source of these oscillations is the interference of time-reversed paths in the InAs shell of our tubular conductor. The observance of a conductance maximum at $B = 0$ implies the presence of spin-orbit coupling via the weak antilocalization effect [27]. In our tubular structures a modulation of the amplitude at $B = 0$ via the time reversal Aharonov-Casher effect was not possible [45], as was demonstrated in arrays of planar ring structures [46]. This is probably due to the tubular geometry of the shell, which has a larger variety of closed-loop trajectories in contrast to averaging interference in an array of planar rings. Additionally, the orientation of the electric field, and thus the precession of the electron spins, differs in our structures compared to planar ring structures. A similar pattern as observed in Figs. 2(f) and 2(j) is found for sample E. Here, the phase-rigid segment also extends to about ± 0.4 T. By comparing the phase rigidity expressed by the standard deviation, it can be concluded that the phase-rigid region of sample E is more robust against averaging over the entire gate voltage range than sample C. Beyond this range, the magnetoconductance oscillations remain to contain an $h/2e$-periodic component, but exhibit random phase shift due to the loss of phase matching along the inner and outer radius of InAs shell [47]. We associate displayed $h/2e$-periodic oscillations beyond ± 0.4 T to the second harmonic of AB oscillations, which may also contribute to a small extent around zero field. The phenomena associated with $h/2e$ oscillations have already been addressed in our recent study of quasiballistic transport properties in phase-pure GaAs/InAs nanowires [10]. In addition to the data presented for samples C and E, $h/2e$-periodic oscillations were also observed for the other samples listed in Table I (see Supplemental Material [44]).

The FFT analysis of the magnetoconductance of samples C and E contains $h/3e$- and $h/4e$-periodic oscillations. Here, we utilize the same approach for extracting these higher-order oscillatory components by selecting frequency windows corresponding to the highlighted regions in the FFT insets. It is important to note that the residual FFT background level was estimated from frequency regions outside the selected harmonic windows and was found to be significantly below the extracted $h/3e$- and $h/4e$-periodic contributions. Additionally, the robustness of the extracted higher-order oscillation components against reasonable variations of the FFT frequency window was systematically verified (see Supplemental Material [44]). Although the extracted amplitudes vary quantitatively with the selected frequency interval owing to the finite width and partial overlap of neighboring FFT peaks, the characteristic phase evolution and the corresponding

physical interpretation remain unchanged. As can be seen in the color map of the $h/3e$-periodic oscillations of sample C in Fig. 2(g), the conductance predominantly exhibits a maximum at $B = 0$ with some short sections of a minimum. Similar to the $h/2e$-periodic oscillations the average value plotted in Fig. 2(k) shows a clear oscillation pattern with a maximum at $B = 0$, which is damped out with increasing field. The $h/3e$-periodic oscillations of sample E shown in Fig. 2(o) reveals an even more stable phase-rigid behavior compared to sample C, with a gradual oscillation amplitude decay with carrier depletion at larger negative gate voltages. As shown in Fig. 2(s) the standard deviation is small in this magnetic field range and also smaller than the standard deviation for sample C given in Fig. 2(k). We assume that the phase rigidity of the $h/3e$-periodic oscillations can be attributed to the propagation of the phase rigidity of the $h/2e$-periodic oscillations, under the premise that the AAS-type oscillations are damped out with an increasing magnetic field, as it is actually observed in Figs. 2(j) and 2(r). Therefore, the conductance is not a periodic function of the magnetic flux (at least for this reason) and then its harmonics are not truly independent. While we cannot rule out a separate interference process with $h/3e$ flux periodicity, we believe the phase rigidity of the $h/3e$-periodic oscillations does not correspond to a distinct physical phenomenon, unlike the phase rigidity of the $h/2e$-periodic oscillations originating from the AAS effect (see Supplemental Material [44]).

For the amplitude of the $h/4e$-periodic oscillations of sample C, the color map shown in Fig. 2(h) reveals a pronounced phase-rigid region approximately half the size of the corresponding $h/2e$-periodic oscillation, and a small standard deviation, shown in Fig. 2(l). Beyond this magnetic field range, the regular phase shifts along the gate voltage range, indicating the previously described phase randomization. As can be inferred from Fig. 2(p), once again for sample E the phase rigidity is more pronounced, supported by the even smaller standard deviation at $B = 0$, shown in Fig. 2(t). The phase rigidity of the $h/4e$-periodic oscillations can be understood within the framework of the AAS-effect when considering quasiclassical trajectories that circumvent the tubular conductor twice for each time-reversed paths thus effectively encircling the magnetic flux four times. This interpretation is supported by the fact that the phase-rigid magnetic field range for the $h/4e$-periodic oscillations is approximately half that for the $h/2e$-periodic oscillations, as seen by comparing Figs. 2(l) and 2(t) with 2(j) and 2(r), which can be explained by the larger phase difference accumulated for inner and out trajectories when circumventing twice. However, our experimental findings of $h/3e$- and $h/4e$-periodic oscillations still remain in need of further analysis. A detailed discussion of results gained through tight-binding model simulations is presented in the following section.

As only three samples of the ones listed in Table I display $h/3e$- and $h/4e$-periodic oscillations, we will limit our understanding of overall tendencies of phase-coherent transport with varying inner contact lengths through more detailed analysis of h/e- and $h/2e$-periodic oscillations. In the following, we focus on the evolution of the relative weights of the h/e and $h/2e$ components as a function of the contact separation length L_c, rather than on their absolute oscillation amplitudes. Even though we expect modest sample-to-sample

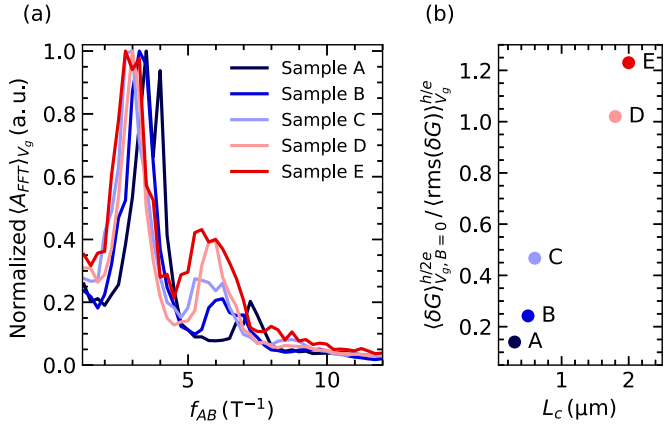

FIG. 3. (a) Normalized average of fast Fourier amplitude $\langle A_{\mathrm{FFT}}\rangle_{V_g}$ as a function of frequency for samples with different contact separations (samples A to E). (b) Ratio of the average amplitude of the AAS oscillations $\langle\delta G\rangle^{h/2e}_{V_g,B=0}$ at $B = 0$ and the root-mean-square amplitude of the h/e-periodic AB-type oscillations, averaged over the gate voltage $\langle\mathrm{rms}(\delta G)\rangle^{h/2e}_{V_g}$ for different contact separation lengths.

disorder configuration and overall core/shell nanowire geometrical variations, we do not expect these to affect evolution of relative contributions of AB and AAS oscillations with increasing measurement segment length L_c. First, comparing the oscillations shown in Figs. 2(e) and 2(m), we observe a tendency for h/e-periodic oscillations amplitude reduction for increasing L_c. This is attributed to an increasing amount of averaging out of non-phase-rigid AB-type oscillations along the nanowire. In Fig. 3(a), the ensemble-averaged normalized FFT spectrum $\langle A_{\mathrm{FFT}}\rangle_{V_g}$ is shown for samples with different contact separation lengths L_c. The normalized FFT spectra reveal how the relative spectral weights of the h/e and $h/2e$ components evolve with increasing L_c. However, since the FFT spectra were taken over the entire magnetic field range of ± 2 T, the $h/2e$-periodic oscillations can originate from the second harmonics of the AB-type oscillations and from the AAS effect. As disclosed earlier in the text, the $h/2e$-periodic oscillations contain a phase-rigid section around $B = 0$, and non-phase-rigid section beyond. To properly discriminate the relationship between the AB and AAS effects, the ratio of the average amplitude of the AAS-type oscillations $\langle\delta G\rangle^{h/2e}_{V_g,B=0}$ at $B = 0$, and the root-mean-square amplitude of the h/e-periodic AB-type oscillations averaged over the gate voltage $\langle\mathrm{rms}(\delta G)\rangle^{h/2e}_{V_g}$ is shown in Fig. 3(b) for varying L_c. It is evident that the ratio increases with increasing contact separation length, indicating an increasing suppression of the AB contribution and a corresponding increase in the relative weight of the phase-rigid AAS contribution. This interpretation is further supported by data on the averaged oscillation amplitude and the extracted FFT peak height of the h/e component given in the Supplemental Material [44].

IV. QUANTUM TRANSPORT SIMULATIONS

To gain a deeper understanding of the interrelation of AB- and AAS-type oscillations for different nanowire lengths, quantum transport simulations were conducted. Details on

the simulation method and parameters are provided in the Supplemental Material [44]. The calculations were performed using the KWANT software package [42]. The assumed radial dimensions of the hexagonally shaped core/shell nanowires were comparable to the experimental ones. Disorder in the wires was described by a Gaussian random field with a disorder strength of 5 meV and a correlation length of 50 nm. Both Rashba spin-orbit coupling and Zeeman splitting were included. Instead of the gate voltage, for the simulations, the chemical potential μ was varied from 10 to 50 meV. We adopt the simplest device model by assuming that the quantum mechanical spectrum itself does not depend on the gate voltage [10]. Indeed, in the real device the gate creates a nonuniform electric field whose variation may also affect all quantum states. However, here we consider these effects negligible. The simulations were performed for a temperature of 1.6 K.

As an initial test, we performed simulations on a 2-μm-long nanowire with and without the presence of spin-orbit coupling. Here, we could observe a clear minimum of conductance at $B = 0$ in the former case, while a maximum was found in the latter case, in accordance with the weak localization and weak antilocalization effects, respectively. More details on this simulation aspect are given in the Supplemental Material [44].

Figure 4 summarizes the simulation results for three different nanowire lengths: 0.6, 2, and 4 μm. The Fourier components related to the periods h/e, $h/2e$, $h/3e$, and $h/4e$ were extracted from the total conductance, interpolated, and plotted as a function of B and μ. Additionally, the corresponding conductance averaged over μ, denoted as $\langle \delta G \rangle_\mu$, and its standard deviation are shown. For all wire lengths, we observe pronounced regular oscillations of the h/e-periodic components of the conductance, with phase shifts as μ is varied, as shown in Figs. 4(a), 4(i), and 4(q). At $B = 0$ the phase switches repeatedly with μ. In our simulations, maxima in δG appear when the density of state possesses a maximum at μ. Standard deviation $\langle \delta G \rangle_\mu$ marked in green for three wire lengths in Figs. 4(e), 4(m), and 4(u) at $B = 0$ implies a positive phase bias, which we attribute to the particular impurity configuration used in our simulation. The $h/2e$-periodic conductance component shown in Figs. 4(b), 4(j), and 4(r), however, exhibits an almost continuous maximum at zero magnetic field for large intervals of the chemical potentials. Still, these intervals are smaller than in the experimental data, most likely because of the limitations of our model. Note that by excluding spin-orbit interaction we could obtain a more extended phase rigidity of the destructive version of the AAS interference (see Supplemental Material [44]). As also observed in the experimental data, the phase-rigid feature persists until larger critical magnetic field with the length of the nanowire, extending over a few units of magnetic flux quantum. Additionally, decrease of standard deviation $\langle \delta G \rangle_\mu$ at $B = 0$ with nanowire length increase, displayed in Figs. 4(f), 4(n), and 4(v), aligns well with our experimental findings given in Fig. 3(b).

In Figs. 4(c) and 4(d), extracted oscillations amplitudes for $h/3e$- and $h/4e$-periodic components of the 600-nm-long nanowire are depicted. However, the extracted average conductance given in Figs. 4(g) and 4(h) give a better qualitative overview, as it showcases a small minimum at zero magnetic field. Nevertheless, the standard deviation is rather large, therefore, we interpret this as an accidental occurrence. In contrast to this, Figs. 4(k) and 4(l), as well as Figs. 4(s) and 4(t), for the 2-μm- and 4-μm-long nanowires exhibit a tendency toward a rigid positive phase at $B = 0$ for both $h/3e$- and $h/4e$-periodic components. Averaged conductance in case of both components presented in Figs. 4(o) and 4(p) for 2-μm-long, and Figs. 4(w) and 4(x) for 4-μm-long nanowires, seems to decrease with increasing nanowire length. However, in case of the $h/3e$-periodic oscillations the standard deviation is relatively large, so the phase rigidity is not as robust as in case of the $h/4e$-periodic oscillations. The latter is not surprising since the $h/4e$-periodic oscillations contain the second harmonics of the phase-rigid $h/2e$-periodic AAS-type oscillations. In addition to that, the phase rigidity of the AAS-type oscillations might also have propagated into the first and third harmonics. This claim is supported by calculation results presented in Supplemental Material [44]. We also tested different disorder potentials and the results were robust. We used multiple random configurations, and we varied the potential amplitude and the correlation length, and the results did not change significantly. This aspect has already been addressed in Ref. [10] (see Figs. S11 and S12 of the corresponding Supplemental Material [44]).

Analogously to the analysis of FFT and oscillation amplitude dependency to varying inner contact length depicted in Fig. 3, we will take a closer look at computed conductance oscillations and its contributions' dependencies to varying nanowire length. In Fig. 5(a) the ensemble-averaged normalized FFT spectra over the chemical potential is shown for the 600-nm-, 2-μm-, and 4-μm-long nanowires (the single spectra for each μ are given in the Supplemental Material [44]). Peaks corresponding to the h/e-, $h/2e$-, $h/3e$-, and $h/4e$-periodic oscillations are clearly resolved, with decreasing peak heights toward higher frequencies. Consistent with the experimental results, we observe that the peak corresponding to the $h/2e$-periodic oscillations is more pronounced for the longer nanowire, confirming the increasingly larger AAS contribution with increasing nanowire length. Finally, Fig. 5(b) depicts the ratio of the average amplitude of the simulated AAS-type oscillations $\langle \delta G \rangle_{\mu,B=0}^{h/2e}$ at $B = 0$ and the root-mean-square amplitude of the h/e-periodic AB-type oscillations averaged over the chemical potential $\langle \mathrm{rms}(\delta G) \rangle_\mu^{h/2e}$ for the 600-nm-, 2-μm-, and 4-μm-long nanowires. In accordance with the experimental results shown in Fig. 3(b), the ratio clearly increases with increasing nanowire length, caused by an increasing averaging out of the AB effect and an enhanced AAS contribution.

V. CONCLUSIONS

We systematically studied flux-periodic oscillations of GaAs/InAs core/shell nanowires at the fundamental period of h/e up to its fourth harmonic $h/4e$. The h/e-periodic oscillations are attributed to the Aharonov-Bohm effect, which is non-phase-rigid for different phase-coherent segments of the nanowire, or when the gate voltage is changed. Nevertheless, even for the longest contact separation length of 2 μm, we found pronounced h/e-periodic oscillations, although with a smaller amplitude, indicating weak disorder-related averaging. This is probably due to the high crystal quality of our

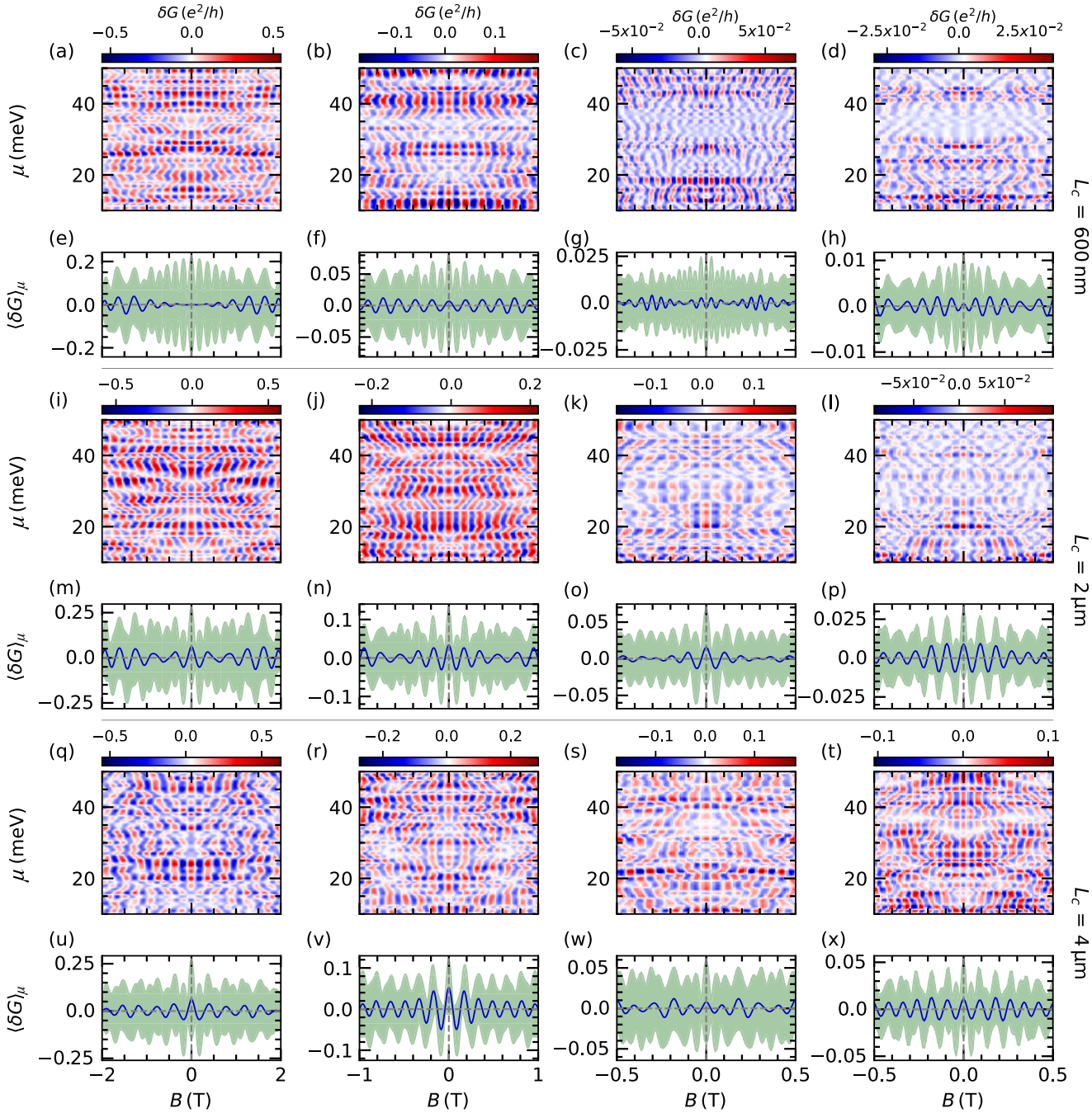

FIG. 4. (a)–(d), (i)–(l), (q)–(t) Show the conductance oscillation amplitudes of first to fourth harmonics, with periods from h/e to $h/4e$, as a function of the magnetic field and chemical potential, for nanowires of lengths $L = 600$ nm, 2 μm, and 4 μm, respectively. (e)–(h), (m)–(p), (u)–(x) Display the average amplitude of the oscillation (solid blue line) and its standard deviation (in green) with respect to the chemical potential μ for each length. Note that the displayed magnetic field range is successively reduced for the higher harmonics.

phase-pure nanowires. In contrast to the averaged oscillation amplitude vanishing for h/e-periodic component, the $h/2e$ oscillations are phase rigid within a certain range around zero field. For these oscillations, phase rigidity increases with longer contact separation, likely due to the diminishing contribution of second harmonics of AB-type oscillations. The latter are visible at larger magnetic fields. Surprisingly, phase rigidity is also observed in the $h/3e$-periodic oscillations, which we could not directly assign to a distinct mechanism based on wave-function interference. Our theoretical analysis suggests that the phase rigidity of the $h/3e$-periodic oscillations is due to the propagation of the phase rigidity of the lower harmonic, i.e., the $h/2e$-periodic AAS-type oscillations and their damping with increasing the magnetic field. We identified a robust phase-rigid magnetic field range for the $h/4e$-periodic oscillations and found that this range is about half as wide as the one of the $h/2e$-periodic oscillations. In general, we can conclude that, despite the short contact separation for some of our nanowires and limited disorder, we clearly observe Altshuler-Aronov-Spivak–type interference effects, which are

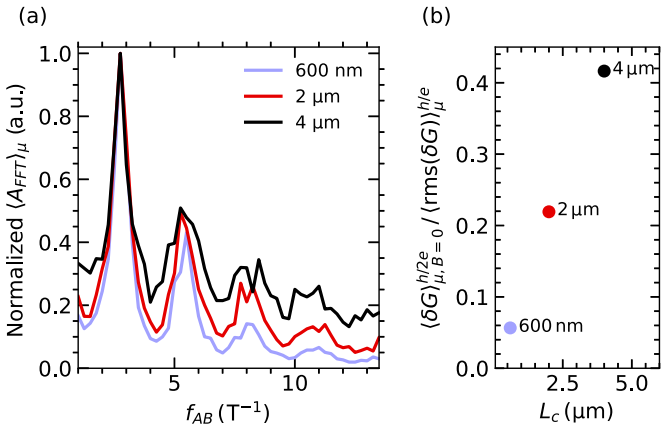

FIG. 5. (a) Normalized fast Fourier amplitude $\langle A_{\mathrm{FFT}}\rangle_\mu$ averaged over μ as a function of frequency f for the 600-nm- (light blue), 2-μm- (red), and 4-μm-long (black) nanowires. (b) Ratio of the average amplitude of the simulated AAS-type oscillations $\langle \delta G\rangle^{h/2e}_{\mu,B=0}$ at $B = 0$ and the root-mean-square amplitude of the simulated h/e-periodic AB-type oscillations averaged over the chemical potential $\langle \mathrm{rms}(\delta G)\rangle^{h/2e}_{\mu}$.

phase rigid and usually attributed to larger ensembles of time-reversed trajectories in the diffusive regime. Our transport simulations investigating the role of increasing wire length also support this conclusion. Another interesting aspect is the occurrence of higher harmonics up to the fourth one. This implies that the conductance oscillations originating from the Aharonov-Bohm effect and weak antilocalization effects deviate from pure sinusoidal dependence. This can be attributed to the quasiballistic transport regime associated with low disorder, which in the semiclassical trajectory picture allows interference of multiple winding paths. In the fully quantum-mechanical picture, one can interpret the presence of higher harmonics that features in the density of states of the nanowire are prevented to be averaged out.

ACKNOWLEDGMENTS

We thank H. Kertz for technical assistance. Dr. F. Lentz and Dr. S. Trellenkamp are gratefully acknowledged for their help with the required e-beam lithography and B. Bennemann for his contribution to the growth of the nanowires. We furthermore thank Dr. K. Moors and W. Schaarman for fruitful discussions and for providing the initial code for the KWANT simulations. The sample fabrication has been performed in the Helmholtz Nano Facility at Forschungszentrum Jülich [48]. This work was partly funded by Deutsche Forschungsgemeinschaft (DFG, German Research Foundation) under Germany's Excellence Strategy—Cluster of Excellence Matter and Light for Quantum Computing (ML4Q) Grant No. EXC 2004/2—390534769. A.M.S. and F.A.C. acknowledge the support of the EPSRC Grant No. EP/W002418/1. T.-G.D. was funded by Reykjavik University Research Fund, Project No. 223016. F.B. and T.S. would like to express their gratitude for the support provided as part of the ASPIRE Project No. JPM-JAP2338.

DATA AVAILABILITY

The data that support the findings of this article are openly available [49].

[1] O. Gül, H. Y. Günel, H. Lüth, T. Rieger, T. Wenz, F. Haas, M. Lepsa, G. Panaitov, D. Grützmacher, and T. Schäpers, Giant magnetoconductance oscillations in hybrid superconductor-semiconductor core/shell nanowire devices, Nano Lett. **14**, 6269 (2014).

[2] K. Gharavi and J. Baugh, Orbital Josephson interference in a nanowire proximity-effect junction, Phys. Rev. B **91**, 245436 (2015).

[3] F. Haas, S. Dickheuer, P. Zellekens, T. Rieger, M. I. Lepsa, H. Lüth, D. Grützmacher, and T. Schäpers, Quantum interferometer based on GaAs/InAs core/shell nanowires connected to superconducting contacts, Semicond. Sci. Technol. **33**, 064001 (2018).

[4] L. Stampfer, D. J. Carrad, D. Olsteins, C. E. N. Petersen, S. A. Khan, P. Krogstrup, and T. S. Jespersen, Andreev interference in the surface accumulation layer of half-shell InAsSb/Al hybrid nanowires, Adv. Mater. **34**, 2108878 (2022).

[5] P. Zellekens, R. S. Deacon, F. Basaric, R. Juluri, M. D. Randle, B. Bennemann, C. Krause, E. Zimmermann, A. M. Sanchez, D. Grützmacher, A. Pawlis, K. Ishibashi, and T. Schäpers, Flux-periodic supercurrent oscillations in an Aharonov–Bohm-type nanowire Josephson junction, Commun. Phys. **8**, 363 (2025).

[6] C. Blömers, T. Rieger, P. Zellekens, F. Haas, M. I. Lepsa, H. Hardtdegen, Ö Gül, N. Demarina, D. Grützmacher, H. Lüth, and T. Schäpers, Realization of nanoscaled tubular conductors by means of GaAs/InAs core/shell nanowires, Nanotechnology **24**, 035203 (2013).

[7] O. Gül, N. Demarina, C. Blömers, T. Rieger, H. Lüth, M. I. Lepsa, D. Grützmacher, and T. Schäpers, Flux periodic magnetoconductance oscillations in GaAs/InAs core/shell nanowires, Phys. Rev. B **89**, 045417 (2014).

[8] F. Haas, T. Wenz, P. Zellekens, N. Demarina, T. Rieger, M. Lepsa, D. Grützmacher, H. Lüth, and T. Schäpers, Angle-dependent magnetotransport in GaAs/InAs core/shell nanowires, Sci. Rep. **6**, 24573 (2016).

[9] F. Haas, P. Zellekens, T. Wenz, N. Demarina, T. Rieger, M. I. Lepsa, D. Grützmacher, H. Lüth, and T. Schäpers, Anisotropic phase coherence in GaAs/InAs core/shell nanowires, Nanotechnology **28**, 445202 (2017).

[10] F. Basarić, V. Brajović, G. Behner, K. Moors, W. Schaarman, A. Manolescu, R. Juluri, A. M. Sanchez, J. H. Bae, H. Lüth, D. Grützmacher, A. Pawlis, and T. Schäpers, Aharonov-Bohm and Altshuler-Aronov-Spivak oscillations in the quasiballistic regime in phase-pure GaAs/InAs core/shell nanowires, Phys. Rev. B **112**, 075301 (2025).

[11] G. de Lange, B. van Heck, A. Bruno, D. J. van Woerkom, A. Geresdi, S. R. Plissard, E. P. A. M. Bakkers, A. R. Akhmerov, and L. DiCarlo, Realization of microwave quantum circuits using hybrid superconducting-semiconducting

nanowire Josephson elements, Phys. Rev. Lett. **115**, 127002 (2015).

[12] T. W. Larsen, K. D. Petersson, F. Kuemmeth, T. S. Jespersen, P. Krogstrup, J. Nygård, and C. M. Marcus, Semiconductor-nanowire-based superconducting qubit, Phys. Rev. Lett. **115**, 127001 (2015).

[13] L. Tosi, C. Metzger, M. F. Goffman, C. Urbina, H. Pothier, S. Park, A. Levy Yeyati, J. Nygård, and P. Krogstrup, Spin-orbit splitting of Andreev states revealed by microwave spectroscopy, Phys. Rev. X **9**, 011010 (2019).

[14] C. Metzger, S. Park, L. Tosi, C. Janvier, A. A. Reynoso, M. F. Goffman, C. Urbina, A. Levy Yeyati, and H. Pothier, Circuit-QED with phase-biased Josephson weak links, Phys. Rev. Res. **3**, 013036 (2021).

[15] P. Zellekens, R. Deacon, P. Perla, D. Grützmacher, M. I. Lepsa, T. Schäpers, and K. Ishibashi, Microwave spectroscopy of Andreev states in InAs nanowire-based hybrid junctions using a flip-chip layout, Commun. Phys. **5**, 267 (2022).

[16] A. Yazdani, F. von Oppen, B. I. Halperin, and A. Yacoby, Hunting for Majoranas, Science **380**, eade0850 (2023).

[17] S. Sarma, M. Freedman, and C. Nayak, Majorana zero modes and topological quantum computation, npj Quantum Inf. **1**, 15001 (2015).

[18] Y. Tserkovnyak and B. I. Halperin, Magnetoconductance oscillations in quasiballistic multimode nanowires, Phys. Rev. B **74**, 245327 (2006).

[19] T. O. Rosdahl, A. Manolescu, and V. Gudmundsson, Spin and impurity effects on flux-periodic oscillations in core-shell nanowires, Phys. Rev. B **90**, 035421 (2014).

[20] G. Ferrari, A. Bertoni, G. Goldoni, and E. Molinari, Cylindrical two-dimensional electron gas in a transverse magnetic field, Phys. Rev. B **78**, 115326 (2008).

[21] A. Manolescu, G. A. Nemnes, A. Sitek, T. O. Rosdahl, S. I. Erlingsson, and V. Gudmundsson, Conductance oscillations of core-shell nanowires in transversal magnetic fields, Phys. Rev. B **93**, 205445 (2016).

[22] Y. Aharonov and D. Bohm, Significance of electromagnetic potentials in the quantum theory, Phys. Rev. **115**, 485 (1959).

[23] B. L. Altshuler, A. G. Aronov, and B. Z. Spivak, The Aaronov-Bohm effect in disordered conductors, Pis'ma Zh. Eksp. Teor. Fiz. **33**, 101 (1981) [JETP Lett. **33**, 94 (1981)].

[24] D. Mailly, C. Chapelier, and A. Benoit, Experimental observation of persistent currents in gaas-algaas single loop, Phys. Rev. Lett. **70**, 2020 (1993).

[25] S. Datta, M. R. Melloch, S. Bandyopadhyay, R. Noren, M. Vaziri, M. Miller, and R. Reifenberger, Novel interference effects between parallel quantum wells, Phys. Rev. Lett. **55**, 2344 (1985).

[26] D. Yu. Sharvin and Yu. V. Sharvin, Quantisation of the magnetic flow in a normal metal cylindrical film, Pis'ma Zh. Eksp. Teor. Fiz. **34**, 285 (1981) [JETP Lett. **34**, 272 (1981)].

[27] A. G. Aronov and Y. V. Sharvin, Magnetic flux effects in disordered conductors, Rev. Mod. Phys. **59**, 755 (1987).

[28] C. P. Umbach, C. Van Haesendonck, R. B. Laibowitz, S. Washburn, and R. A. Webb, Direct observation of ensemble averaging of the Aharonov-Bohm effect in normal-metal loops, Phys. Rev. Lett. **56**, 386 (1986).

[29] L. P. Lévy, G. Dolan, J. Dunsmuir, and H. Bouchiat, Magnetization of mesoscopic copper rings: Evidence for persistent currents, Phys. Rev. Lett. **64**, 2074 (1990).

[30] V. Chandrasekhar, R. A. Webb, M. J. Brady, M. B. Ketchen, W. J. Gallagher, and A. Kleinsasser, Magnetic response of a single, isolated gold loop, Phys. Rev. Lett. **67**, 3578 (1991).

[31] J. Dauber, M. Oellers, F. Venn, A. Epping, K. Watanabe, T. Taniguchi, F. Hassler, and C. Stampfer, Aharonov-Bohm oscillations and magnetic focusing in ballistic graphene rings, Phys. Rev. B **96**, 205407 (2017).

[32] A. Bachtold, C. Strunk, J.-P. Salvetat, J.-M. Bonard, L. Forró, T. Nussbaumer, and C. Schönenberger, Aharonov–Bohm oscillations in carbon nanotubes, Nature (London) **397**, 673 (1999).

[33] P. Zellekens, N. Demarina, J. Janßen, T. Rieger, M. Ion Lepsa, P. Perla, G. Panaitov, H. Lüth, D. Grützmacher, and T. Schäpers, Phase coherent transport and spin-orbit interaction in GaAs/InSb core/shell nanowires, Semicond. Sci. Technol. **35**, 085003 (2020).

[34] M. Jung, J. S. Lee, W. Song, Y. H. Kim, S. D. Lee, N. Kim, J. Park, M.-S. Choi, S. Katsumoto, H. Lee, and J. Kim, Quantum interference in radial heterostructure nanowires, Nano Lett. **8**, 3189 (2008).

[35] H. Peng, K. Lai, D. Kong, S. Meister, Y. Chen, X.-L. Qi, S.-C. Zhang, Z.-X. Shen, and Y. Cui, Aharonov-Bohm interference in topological insulator nanoribbons, Nat. Mater. **9**, 225 (2010).

[36] S. Cho, B. Dellabetta, R. Zhong, J. Schneeloch, T. Liu, G. Gu, M. J. Gilbert, and N. Mason, Aharonov-Bohm oscillations in a quasi-ballistic three-dimensional topological insulator nanowire, Nat. Commun. **6**, 7634 (2015).

[37] Y. C. Arango, L. Huang, C. Chen, J. Avila, M. C. Asensio, D. Grützmacher, H. Lüth, J. G. Lu, and T. Schäpers, Quantum transport and nano angle-resolved photoemission spectroscopy on the topological surface states of single Sb_2Te_3 nanowires, Sci. Rep. **6**, 29493 (2016).

[38] D. Rosenbach, N. Oellers, A. R. Jalil, M. Mikulics, J. Kölzer, E. Zimmermann, G. Mussler, S. Bunte, D. Grützmacher, H. Lüth, and T. Schäpers, Quantum transport in topological surface states of selectively grown Bi_2Te_3 nanoribbons, Adv. Electron. Mater. **6**, 2000205 (2020).

[39] H.-S. Kim, T.-H. Hwang, N.-H. Kim, Y. Hou, D. Yu, H.-S. Sim, and Y.-J. Doh, Adjustable quantum interference oscillations in Sb-doped Bi_2Se_3 topological insulator nanoribbons, ACS Nano **14**, 14118 (2020).

[40] A. E. Hansen, A. Kristensen, S. Pedersen, C. B. Sørensen, and P. E. Lindelof, Mesoscopic decoherence in Aharonov-Bohm rings, Phys. Rev. B **64**, 045327 (2001).

[41] J. Dufouleur, L. Veyrat, A. Teichgräber, S. Neuhaus, C. Nowka, S. Hampel, J. Cayssol, J. Schumann, B. Eichler, O. G. Schmidt, B. Büchner, and R. Giraud, Quasiballistic transport of Dirac fermions in a Bi_2Se_3 nanowire, Phys. Rev. Lett. **110**, 186806 (2013).

[42] C. W. Groth, M. Wimmer, A. R. Akhmerov, and X. Waintal, Kwant: A software package for quantum transport, New J. Phys. **16**, 063065 (2014).

[43] M. M. Jansen, P. Perla, M. Kaladzhian, N. von den Driesch, J. Janßen, M. Luysberg, M. I. Lepsa, D. Grützmacher, and A. Pawlis, Phase-pure wurtzite GaAs nanowires grown by self-catalyzed selective area molecular beam epitaxy for advanced laser devices and quantum disks, ACS Appl. Nano Mater. **3**, 11037 (2020).

[44] See Supplemental Material at http://link.aps.org/supplemental/10.1103/5x9w-pjtq for experimental details, transmission

electron microscopy studies, h/e and higher harmonics conductance contributions of all samples, extracted oscillation amplitudes, data processing, simulations, and modeling, which include Refs. [50–52].

[45] Y. Aharonov and A. Casher, Topological quantum effects for neutral particles, Phys. Rev. Lett. **53**, 319 (1984).

[46] T. Bergsten, T. Kobayashi, Y. Sekine, and J. Nitta, Experimental demonstration of the time reversal Aharonov-Casher effect, Phys. Rev. Lett. **97**, 196803 (2006).

[47] L. C. Mur, C. J. P. M. Harmans, and W. G. van der Wiel, Competition between h/e and $h/2e$ oscillations in a semiconductor Aharonov–Bohm interferometer, New J. Phys. **10**, 073031 (2008).

[48] W. Albrecht, J. Moers, and B. Hermanns, HNF-Helmholtz nano facility, JLSRF **3**, A112 (2017).

[49] F. Basarić, K. Wang, T.-G. Dumitru, A. Manolescu, F. Alvarado-Cesar, A. M. Sanchez, D. Grützmacher, A. Pawlis, and T. Schäpers, Data for: Interplay between Aharonov–Bohm and Altshuler–Aronov–Spivak oscillations in phase-pure GaAs/InAs core/shell nanowires of different lengths, JülichDATA (2026).

[50] G. J. Dolan, J. C. Licini, and D. J. Bishop, Quantum interference effects in lithium ring arrays, Phys. Rev. Lett. **56**, 1493 (1986).

[51] A. Ballester, C. Segarra, A. Bertoni, and J. Planelles, Suppression of the Aharonov-Bohm effect in hexagonal quantum rings, Europhys. Lett. **104**, 67004 (2013).

[52] M. Urbaneja Torres, A. Sitek, S. I. Erlingsson, G. Thorgilsson, V. Gudmundsson, and A. Manolescu, Conductance features of core-shell nanowires determined by their internal geometry, Phys. Rev. B **98**, 085419 (2018).